Multiband optical variability of 3C 279 on diverse time-scales

Aditi Agarwal,[1]⋆ Sergio A. Cellone,[2,3]⋆ Ileana Andruchow,[4] Luis Mammana,[3]
Mridweeka Singh,[5] G. C. Anupama,[1] B. Mihov,[6] Ashish Raj,[1] L. Slavcheva-Mihova,[6]
Aykut Özdönmez[7] and Ergün Ege[8]

[1]*Indian Institute of Astrophysics, Block II, Koramangala, Bangalore 560034, India*
[2]*Facultad de Ciencias Astronómicas y Geofísicas, Universidad Nacional de La Plata, Paseo del Bosque S/N, B1900 FWA, La Plata, Argentina*
[3]*Complejo Astronómico 'El Leoncito' (CASLEO), CONICET–UNLP–UNC–UNSJ, España 1512 (Sur), J5402DSP, San Juan, Argentina*
[4]*Instituto de Astrofísica de La Plata (CCT La Plata–CONICET–UNLP), Calle 8 1467, B1904CMC, La Plata, Argentina*
[5]*Aryabhatta Research Institute of Observational Sciences (ARIES), Manora Peak, Nainital 263002, India*
[6]*Institute of Astronomy and NAO, Bulgarian Academy of Sciences, 72 Tsarigradsko Chaussee Blvd., 1784 Sofia, Bulgaria*
[7]*TÜBİTAK National Observatory, Akdeniz University Campus, Antalya 07058, Turkey*
[8]*Graduate School of Science and Engineering, Istanbul University, Beyazit, Istanbul 34116, Turkey*

ABSTRACT

We have monitored the flat spectrum radio quasar, 3C 279, in the optical *B*, *V*, *R*, and *I* passbands from 2018 February to 2018 July for 24 nights, with a total of 716 frames, to study flux, colour, and spectral variability on diverse time-scales. 3C 279 was observed using seven different telescopes: two in India, two in Argentina, two in Bulgaria, and one in Turkey to understand the nature of the source in optical regime. The source was found to be active during the whole monitoring period and displayed significant flux variations in *B*, *V*, *R*, and *I* passbands. Variability amplitudes on intraday basis varied from 5.20 to 17.9 per cent. A close inspection of variability patterns during our observation cycle reveals simultaneity among optical emissions from all passbands. During the complete monitoring period, progressive increase in the amplitude of variability with frequency was detected for our target. The amplitudes of variability in *B*, *V*, *R*, and *I* passbands have been estimated to be 177 per cent, 172 per cent, 171 per cent, and 158 per cent, respectively. Using the structure function technique, we found intraday time-scales ranging from ∼23 min to about 115 min. We also studied colour–magnitude relationship and found indications of mild bluer-when-brighter trend on shorter time-scales. Spectral indices ranged from 2.3 to 3.0 with no clear trend on long-term basis. We have also generated spectral energy distributions for 3C 279 in optical *B*, *V*, *R*, and *I* passbands for 17 nights. Finally, possible emission mechanisms causing variability in blazars are discussed briefly.

Key words: galaxies: active – BL Lacertae objects: general – BL Lacertae objects: individual: 3C 279 – quasars: individual.

1 INTRODUCTION

The term active galactic nuclei (AGNs) is used to describe small bright regions in the centre of certain galaxies with characteristic bolometric luminosities ranging between 10^{41} and 10^{48} erg s^{-1}. AGNs are believed to be powered by an actively accreting and possibly spinning central supermassive black hole (SMBH; Begelman, Blandford & Rees 1984). AGNs are known to host SMBHs with masses ranging from 10^6 to 10^{10} M$_\odot$. The central SMBH accretes

matter due to its strong gravitational forces and surrounding it is an optically thick, geometrically thin accretion disc (AD) formed due to the loss of angular momentum through viscous and turbulent processes coming into play during accretion (Shakura & Sunyaev 1973). The AD emits mainly in optical, UV, and soft X-ray bands of the electromagnetic (EM) spectrum. In addition to the central SMBH and the AD, the canonical model of an AGN consists of a dusty torus surrounding the central region, an X-ray emitting corona, and relativistic bipolar outflows (Blandford & Königl 1979). A special class of AGNs having relativistic jets pointing towards the observer are known as blazars. Blazars are characterized by strong emission violently variable over the entire EM spectrum and also apparent superluminal motions. They are also the dominant

sources for gamma-ray emission in the sky (Acero et al. 2015). Blazars have been classified into BL Lac objects (BL Lacs) and flat spectrum radio quasars (FSRQs) based on their optical spectra (Giommi et al. 2012). A high degree of linear polarization at optical wavelengths has been reported for some blazars, including 3C 279 (Blinov et al. 2015). Andruchow et al. (2003) detected strong microvariability of ∼10 per cent in the linear polarization of 3C 279 observed in *V* passband. Blazars have their jet axis aligned at angles ≤10° to the observer's line of sight (LOS; e.g. Urry & Padovani 1995) that along with the relativistic beaming leads to above observational features of blazars. It is generally believed that the jet alignment increases the amplitude of the emission and contracts the variability time-scale. Blazars have been known to vary throughout the EM spectrum over diverse time-scales ranging from few min to years (Fan et al. 2005). Blazars variability has been broadly divided into three classes: magnitude changes of upto few tenths over a time-scale of few min to day or less are considered to be intraday variability (IDV; Wagner & Witzel 1995; Xie, Zhou & Liang 2004) or microvariability, flux changes typically exceeding ∼1 mag over several days to months are known as short-term variability (STV), while the changes over several months to years (sometimes can exceed even ∼5 mag) are grouped under long-term variability (LTV; Fan & Lin 2000; Gupta et al. 2004).

The spectral energy distribution (SED) of blazars is characterized by two broad bumps: a low-energy one due to synchrotron radiation, which covers the radio to the X-ray range, and a high-energy one due to inverse Compton (IC) emission, which covers from the X-rays to the γ-rays. According to the leptonic jet models, the low-frequency emission can be explained as synchrotron emission from non-thermal electrons. On the other hand, the high-energy radiation can be associated with the IC scattering of low-energy synchrotron photons from the jet (synchrotron self-Compton; König 1981), and/or with the thermal photons outside the jet (external Compton; Hunger & Reimer 2016). The SEDs of blazars can also be generated using other models, e.g. hadronic or lepto-hadronic emission models (e.g. Mücke et al. 2003; Böttcher et al. 2013). SEDs are helpful in identifying the contributions of emission from synchrotron mechanism, dust, broad-line region, AD, star light, and surrounding regions.

3C 279 is a well-studied blazar (e.g. Maraschi et al. 1994; Wehrle et al. 1998; Lindfors et al. 2006; Collmar et al. 2007) that has shown multiwavelength flux variability. It is the first extragalactic radio source that showed superluminal motion (Cohen et al. 1971). 3C 279 is a luminous FSRQ at $z = 0.536$ (Lynds, Stockton & Livingston 1965) with the central black hole mass in the range of $(3–8) \times 10^8$ M$_\odot$ (Gu, Cao & Jiang 2001; Woo & Urry 2002; Nilsson et al. 2009). It is also the first FSRQ detected in very high energy (VHE) γ-rays by the Major Atmospheric Gamma-ray Imaging Cherenkov (MAGIC) Telescope (MAGIC Collaboration 2008). Extensive monitoring with high-resolution very long baseline interferometry (VLBI) observations revealed many important results for this source, e.g. a one-sided jet extending south-west on pc-scale characterized by bright knots ejected from the core region (see Unwin et al. 1989; Wehrle et al. 2001; Jorstad et al. 2005; Chatterjee et al. 2008). The electric field vector was found to be aligned with the jet direction in VLBA polarimetry observations, which indicate that the magnetic field was predominantly perpendicular to the relativistic jets. The important parameters, e.g. bulk Lorentz factor, viewing angle of the jet flow, were estimated as $\Gamma_j = 13.3 \pm 0.6$ and $\Theta_j = 1.9° \pm 0.6°$ from very long baseline array (VLBA) radio observations (Jorstad et al. 2017).

Blazar variability studies can provide information on the dominant emission mechanism behind observed manifestations that in turn can shed light on various theoretical models. Variability studies of blazars have been conducted by optical astronomers around the world for over 50 yr, but some pertinent questions still remain unresolved. To further understand the characteristics of 3C 279, we here study its variability properties on diverse time-scales in optical *B*, *V*, *R*, and *I* bands. The photometric data have been obtained from seven different optical telescopes around the world during 2018 in *B*, *V*, *R*, and *I* passbands. We have also investigated SEDs of the target in the optical regime. This paper is structured as follows. Section 2 gives an overview of the multiband observations used and data-reduction procedure. In Section 3, various analysis techniques are introduced. Section 4 gives results, discussion is given in Section 5, and conclusions are given in Section 6.

2 OBSERVATIONS AND DATA REDUCTION

For this study, observations covering optical *B*, *V*, *R*, and *I* passbands were performed for the blazar 3C 279, from 2018 February to 2018 July. Our photometric observations were performed using seven optical telescopes around the world that are briefly described below.

We carried our optical *B*, *V*, *R*, and *I* observations using the 2.01-m optical-infrared Himalayan Chandra Telescope (HCT; Telescope A of Table 1) located at Indian Astronomical Observatory, Hanle (latitude 32° 46′ N, longitude 78° 57′ E, altitude 4500 m), India, remotely operated from Centre for Research and Education in Science & Technology (CREST), Hosakote, via a dedicated satellite link. It has a Ritchey-Chrétien (RC) optics with an altitude over azimuth mount. Observations were performed with the Hanle Faint Object Spectrograph Camera (HFOSC) mounted on HCT and equipped with 2k × 4k SITe ST-002 CCD. The central region of 2k × 2k with a plate scale of 0.296 arcsec pixel^{-1} corresponds to a field of 10 arcmin × 10 arcmin. More details are given in Table 1. We have also used 1.3-m Devasthal Fast Optical Telescope (DFOT) of ARIES (Telescope B of Table 1), Nainital with latitude 29° 21′ N, longitude 79° 41′ E, altitude 2420 m operated by ARIES, Nainital, India. The 1.3-m DFOT has fork equatorial-type mount system and a fast beam with a focal ratio *f*/4 that provides 40 arcsec sky view in 1-mm scale at the focal plane. It is equipped with Andor 2K × 2K CCD with 13.5-μm pixel size, 512 × 512 CCD with 16-μm pixel size, and also a 3326 × 2504 CCD with 5.4-μm pixel size. For our observations, we have used 512 × 512 CCD. Sky brightness as measured on a moonless night in the *V* passband is ∼21.2 mag arcsec^{-2} that varies with the Moon's phase. It uses RC Cassegrain design and has a field of view of 5.4 arcsec. In addition to the above two telescopes, optical observations of 3C 279 were also obtained with two different telescopes at CASLEO (Argentina): the Helen Sawyer Hogg (HSH; Telescope E of Table 1) 0.6 -m Telescope (on loan from the University of Toronto, Canada), and the Jorge Sahade (JS; Telescopes C and D of Table 1) 2.15-m Telescope. HSH is equipped with a SBIG STL-1001E CCD camera, while two different Nitrogen-cooled CCDs were used at the JS: a Tektronix TK1024, and a Roper Versarray 2048B. Standard Johnson (BV) − Cousins (RI) filter sets were used at both telescopes. Furthermore, observations of 3C 279 were also obtained using the 2-m *f*/8 RC (Telescope F of Table 1) and the 50/70-cm *f*/3.44 Schmidt (Telescope G of Table 1) telescopes of the Rozhen National Astronomical Observatory, Bulgaria, during the period 2018 March 15 to 2018 May 14. The two-channel focal reducer FoReRo-2

Table 1. Details of telescopes and instruments.

Site:	A	B	C	D	E	F	G	H
Telescope	2.01-m RC	1.30-m RC Cassegrain	2.15 m RC Nasmyth	2.15 m RC Cassegrain	0.6 m classic Cassegrain	2-m Ritchey-Chrétien+FoReRo-2 focal reducer	50/70-cm Schmidt	0.6m RC Cassegrain
CCD model	SITe ST-002	Andor 512 × 512	Roper Scientific Versarray 2048B (cooling: liquid N2)	TK1024 (cooling: liquid N2)	SBIG STL–1001E (cooling: Peltier)	VersArray:1300B	FLI PL16803	Apogee Alta U42 CCD
Chip size (pixels)	2048 × 2048	512 × 512	2048 × 2048	1024 × 1024	1024 × 1024	1340 × 1300	4096 × 4096	2048 × 2048
Pixel size (μm)	15 × 15	16 × 16	13.5 × 13.5	24 × 24	24 × 24	20.0 × 20.0	9 × 9	13.5 × 13.5
Scale (arcsec pixel^{-1})	0.296	0.63	0.45	0.27 (unbinned)	0.54 (unbinned)	0.737	1.079	0.58
Field	10 arcmin × 10 arcmin	5.4 arcmin × 5.4 arcmin	9 arcmin diameter	5 arcmin diameter	9.3 arcmin × 9.3 arcmin	16.5 arcmin × 16 arcmin	73.7 arcmin × 73.7 arcmin	19.8 arcmin × 19.8 arcmin
Gain	$1.22\,e^-$/ADU	$1.4\,e^-$/ADU	$2.18\,e^-$/ADU	$1.98\,e^-$/ADU	$2.2e^-$/ADU	$1.0e^-$/ADU	$1.49\,e^-$/ADU	$1.19\,e^-$/ADU
Read Out Noise	$4.87\,e^-$ rms	$6.0\,e^-$ rms	$3.1\,e^-$ rms	$7.40\,e^-$ rms	$14.8\,e^-$ rms	$2.0\,e^-$ rms	$8.97\,e^-$ rms	$11.0\,e^-$ rms
Binning used	1 × 1	1 × 1	1 × 1	2 × 2	1 × 1	1 × 1	1 × 1	1 × 1
Typical seeing (arcsec)	1–3	1–3	1.8–2.5	1.8–2.5	1.2–2.2	1.5–2.5	2.0–3.0	1.5–2.5

Notes. A : 2.01-m RC Himalayan Chandra Telescope (HCT) at Indian Astronomical Observatory, Hanle, India.
B: 1.30-m RC Cassegrain Optical Telescope, ARIES, Nainital, India.
C, D: 2.15-m RC Nasmyth at CASLEO, Argentina.
E: 0.6-m Classic Cassegrain at CASLEO, Argentina.
F: 2-m RC Telescope at National Astronomical Observatory Rozhen, Bulgaria.
G: 50/70-cm Schmidt Telescope at National Astronomical Observatory, Rozhen, Bulgaria.
H: 0.6-m RC Cassegrain Telescope at Ulupinar Observatory Operated by Istanbul University, Turkey.

(Jockers et al. 2000) was attached to the RC focus of the 2-m Telescope which yields a focal ratio of *f*/2.8. Both telescopes are equipped with CCD cameras and a standard Johnson–Cousins *BVRI* set of filters. Each 3C 279 observing set consists of several exposures through the *R* filter (the 2-m Telescope data) or *BVRI* filters (the Schmidt Telescope data; only the central 1024 × 1024 pixels of the CCD were actually used). Observation of 3C 279 on 2018 May 13–14 made use of the 0.6-m Telescope (IST60; Telescope H of Table 1) at Ulupinar observatory operated by Istanbul University in Turkey. The telescope is equipped with an Apogee CCD detector and Bessel *UBVRI* filters. Further details of telescopes used are given in Table 1.

CCD images of our source obtained using above telescopes are raw frames that could be affected and deformed by the atmospheric effects or bad focusing. So, to extract useful information they were subjected to pre-processing, processing, and post-processing. The CCD images obtained with the above-mentioned telescopes were de-biased and flat-fielded using standard procedures. Finally, all source images were corrected for cosmic rays. Above steps were performed using IRAF[1] software. The next stage in data reduction is processing that includes extraction of target's position and magnitude from the rectified CCD intensity array using the Dominion Astronomical Observatory Photometry (DAOPHOT II) software (Stetson 1987, 1992). Aperture photometry was performed using DAOPHOT II for four aperture radii, i.e. ∼1 × FWHM, 2 × FWHM, 3 × FWHM, and 4 × FWHM, out of which aperture 2 × FWHM was selected to get instrumental magnitude of the source, as it showed the best S/N ratio. In addition to above two softwares, MATLAB was used to write any additional program used in data analysis.

For our source 3C 279, we selected three local standard stars from the observed frame. Instrumental magnitudes of the target plus these standard stars were extracted using the process described above. Of these three stars, we finally selected two standard stars with magnitudes similar to our source and also in its close proximity. Since we have selected the target and the standard star from the same field, the air mass along with the instrumental and weather conditions are the same, making the flux ratios very reliable. The complete observation log is given in Table 2, where column 1 gives the observation date, column 2 reports the telescope used, and column 3 states the number of frames observed in each frame for the respective observation date. On almost every observation date, we took quasi-simultaneous single data points in *B*, *V*, *R*, and *I* filters.

3 ANALYSIS TECHNIQUES

To quantify optical variability in the light curves (LCs) of the source, we have employed three statistics (e.g. de Diego 2010), namely the *C*-, *F*-, and χ^2-tests. Given the modest number of observations, we opted to use the *C*-, *F*-, and χ^2-tests.

3.1 *C*-Test

The *C*-statistic, introduced by Romero, Cellone & Combi (1999), is the most frequently used criterion to claim the variability of the

Table 2. Log of photometric observations of 3C 279.

Date of observations (yyyy mm dd)	Telescope	Number of data points			
		B	*V*	*R*	*I*
2018 02 08	C	0	0	36	0
2018 02 17	A	1	1	47	1
2018 02 18	A	1	1	1	1
2018 02 21	A	1	1	57	1
2018 03 15	G	3	1	3	2
2018 03 26	E	4	4	5	6
2018 03 28	D	2	4	4	3
2018 04 16	B	2	2	49	2
2018 04 17	B	1	1	53	1
2018 04 18	B	0	0	102	0
2018 04 20	E	0	7	7	7
2018 04 21	E	0	8	8	8
2018 04 21	F	0	0	3	0
2018 04 22	F	0	0	3	0
2018 04 23	G	1	2	2	2
2018 04 23	E	0	3	2	2
2018 05 05	B	1	2	86	2
2018 05 06	B	2	2	80	2
2018 05 13	H	0	0	23	17
2018 05 13	G	1	1	2	2
2018 05 14	F	0	0	3	0
2018 05 18	A	1	1	1	1
2018 05 19	A	1	1	1	1
2018 07 08	D	0	6	4	3

source. The variability detection parameter, *C*, is defined as the average of C_1 and C_2 with

$$C_1 = \frac{\sigma(\mathrm{BL} - S_A)}{\sigma(S_A - S_B)}, \quad C_2 = \frac{\sigma(\mathrm{BL} - S_B)}{\sigma(S_A - S_B)}. \tag{1}$$

Here, $(\mathrm{BL} - S_A)$, $(\mathrm{BL} - S_B)$, and $(S_A - S_B)$ are the differential instrumental magnitudes of the blazar and standard star A (S_A), the blazar and standard star B (S_B), and S_A versus S_B calculated using aperture photometry of the source and comparison stars, while $\sigma(\mathrm{BL} - S_A)$, $\sigma(\mathrm{BL} - S_B)$, and $\sigma(S_A - S_B)$ are observational scatters of the differential instrumental magnitudes of the blazar $- S_A$, blazar $- S_B$, and $S_A - S_B$, respectively. Zibecchi et al. (2017) analysed IDV in AGNs using different statistical methods currently used in the literature. Through their study they concluded that even though the C statistics cannot be considered as a genuine statistical test, it could nevertheless be a suitable parameter to detect variability with more reliable results as compared to *F*-test.

An LC is considered to be variable at a nominal confidence level of >99 per cent when $C \geq 2.57$ else we call it non-variable (NV).

3.2 *F*-Test

As mentioned by de Diego (2010), the *F*-test is considered to be a powerful and properly distributed statistic, which is used to quantify the variability nature of sources. The *F*-values compare two sample variances and are given as

$$F_1 = \frac{\sigma^2(\mathrm{BL} - S_A)}{\sigma^2(S_A - S_B)}, \qquad F_2 = \frac{\sigma^2(\mathrm{BL} - S_B)}{\sigma^2(S_A - S_B)}. \tag{2}$$

Here, $(\mathrm{BL} - S_A)$, $(\mathrm{BL} - S_B)$, and $(S_A - S_B)$ are the differential instrumental magnitudes of blazar and standard A, blazar and standard B, and standard A and standard B, respectively, computed using the aperture photometry technique, while $\sigma^2(\mathrm{BL} - S_A)$, $\sigma^2(\mathrm{BL} - S_B)$, and $\sigma^2(S_A - S_B)$ are the variances of differential

instrumental magnitudes. Averaging F_1 and F_2 gives the mean observational F value which is then compared with the critical value, $F_{\nu_{bl}, \nu_*}^{(\alpha)}$, where ν_{bl} and ν_* express the number of degrees of freedom for the blazar and star, respectively, calculated as the number of measurements, N, minus 1 ($\nu = N - 1$), while α is the significance level set as 0.1 and 1 per cent (i.e. 3σ and 2.6σ) in this study. If the mean F-value is larger than the critical value (F_c), the null hypothesis (i.e. that of no variability) is rejected.

3.3 χ^2-test

To investigate the presence or absence of variability in our target, we also implemented the χ^2-test that is interpreted as

$$\chi^2 = \sum_{i=1}^{N} \frac{(V_i - \overline{V})^2}{\sigma_i^2}, \tag{3}$$

where $\overline{V}$ is the mean magnitude and the ith observation yields a magnitude V_i with a corresponding standard error σ_i. This error can be attributed to photon noise from the source and sky, CCD read-out, and other non-systematic causes. Calculating exact values of such errors by the IRAF data analysis package is unattainable. Theoretical errors have been found to be smaller than the real errors by a factor of 1.3–1.75 (e.g. Gopal-Krishna et al. 2003) which for our data is around 1.6, on average. Thus, the errors obtained after data analysis should be multiplied by the above factor to get better estimation of the real photometric errors. This statistic is then compared with a critical value $\chi^2_{\alpha, \nu}$ where α is the significance level similar to that of the F-test and $\nu = N - 1$ is the degree of freedom. $\chi^2 > \chi^2_{\alpha, \nu}$ implies the presence of variability.

3.4 Percentage amplitude variation

To characterize the variability of the source in all LCs, we calculated the variability amplitude parameter A introduced by Heidt & Wagner (1996), and defined as

$$A = 100 \times \sqrt{(A_{max} - A_{min})^2 - 2\sigma^2} \text{ (per cent)}, \tag{4}$$

where A_{max} and A_{min} are the maximum and minimum values in the differential LCs of the blazar, and σ is the average measurement error.

3.5 Structure function

The structure function (SF) provides information about the statistical nature of time-series. It is especially well adapted to quantitatively calculate periodicity and time-scales that contribute to fluctuations, thus providing information on the underlying cause of variability. The SF has been introduced and discussed at length by Simonetti, Cordes & Heeschen (1985). It is not affected by any data gaps in the LCs and can be applied to unevenly sampled data.

First-order SF for a data series is defined as

$$SF(\tau_j) = \frac{1}{N(\tau)} \sum_{i=1}^{N} \omega(i)\omega(i + \tau)[a(i) - a(i + \tau_j)]^2, \tag{5}$$

where τ is the time lag. The weighting function $\omega(i)$ is 1 if we have observations for the ith interval, else it is 0. Further details on the SF can be found in Gaur et al. (2010) and Agarwal et al. (2015). For a sinusoidal time-series with period P, the SF curve has minima at τ equal to the period (P) and its sub-harmonics (e.g. Lachowicz, Czerny & Abramowicz 2006).

3.6 Discrete correlation function

To quantify the presence of a periodic signal in the LC of 3C 279, if any, we first used the Discrete Correlation Function (DCF) technique proposed by Edelson & Krolik (1988). It permits to study a correlative relationship between any two data sets. For two discrete data sets (a_i, b_j), we first calculated the unbinned DCF (UDCF) as

$$UDCF_{ij}(\tau) = \frac{(a_i - \bar{a})(b_j - \bar{b})}{\sqrt{(\sigma_{a^2} - e_{a^2})(\sigma_{b^2} - e_{b^2})}}, \tag{6}$$

where $\bar{a}, \bar{b}$ are the mean values of two data sets; σ_a, σ_b are their standard deviations; and e_a, e_b are measurement errors of data points in the two data series. Each value of UDCF is associated with a time delay $\Delta t_{ij} = (t_{bj} - t_{ai})$. The DCF is obtained by averaging the UDCF values for each time lag τ over the interval $\tau - \frac{\Delta\tau}{2} \leq t_{ij} \leq \tau + \frac{\Delta\tau}{2}$ as following:

$$DCF(\tau) = \frac{\sum_{k=1}^{m} UDCF_k}{M}, \tag{7}$$

where M is the number of pairs with time lag values lying in the τ interval. Errors in DCF are calculated using the formula:

$$\sigma_{DCF(\tau)} = \frac{\sqrt{\sum_{k=1}^{M}(UDCF_k - DCF(\tau))^2}}{M - 1}. \tag{8}$$

As the two series that were correlated were identical, we obtained the discrete autocorrelation function (DACF) that was then used to search for periodicity. The essence of DACF is that for clear correlation, the DACF peaks at time lags equal to zero, and the presence of periodicity in the LC will appear as secondary peaks in DACF.

4 RESULTS

Observations of the blazar were carried out for 24 nights between 2018 February and 2018 July. Observation log is given in Table 2. To investigate IDV properties, we observed the blazar for $\sim$3–5 h in R band on a total of nine nights. Calibrated intraday LCs for our source are shown in Fig. 1. In order to statistically examine R-band intraday LCs for presence or absence of variations, we performed C-test, F-test, and χ^2-tests as discussed in Sections 3.1–3.3, respectively. The LC of the blazar is considered as variable (Var) when variability conditions for all the tests are met at the 0.999 level and is said to be NV if none of these conditions are met. The source was found to be active during the entire monitoring period. Owing to small field of view, out of nine nights, we were not able to perform variability detection tests on 2018 February 08 and 2018 April 18 LCs as we had insufficient standard stars in the field. Following above criteria, we found the source to be variable on five nights i.e. 2018 February 17, 21, April 17, and May 05 and 06. To calibrate the blazar LC of April 18, we found star 1[2] appropriate to be used as standard comparison star. Variability amplitude for April 18 LC was found to be 17.90 per cent and the LC for the same is displayed in Fig. 1. Variability amplitudes for our five IDV nights during which the source was found to be variable ranged from 5.20 per cent to 13.90 per cent. IDV LCs of 3C 279 in Fig. 1 illustrate that the source displayed rise and fall in flux levels on many instances during 3–4 h of continuous monitoring, thus indicating towards the presence of characteristic time-scale of variations. IDV results and variability amplitudes are listed in Table 3, where column 1 gives observation

[2]https://www.lsw.uni-heidelberg.de/projects/extragalactic/charts/1253-055.html
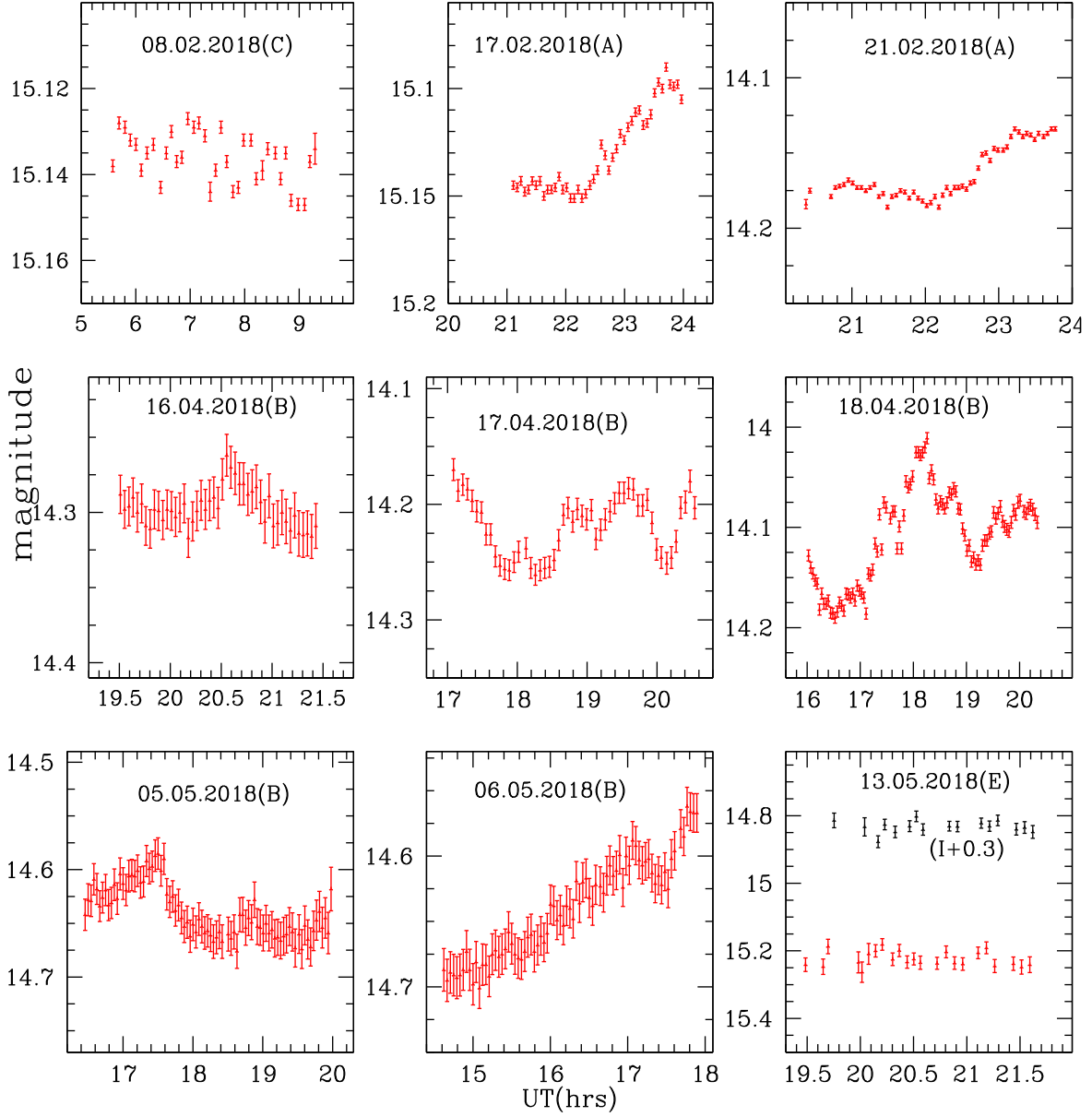
Figure 1. LCs for 3C 279; red denotes *R* filter while black denotes *I* filter. In each plot, *x*- and *y*-axes are the UT and magnitude, respectively. Observation date and the telescope used are indicated in each plot.

Table 3. Results of IDV observations of 3C 279.

Date (yyyy mm dd)	Band	N	C-test C_1, C_2, C	F-test $F_1, F_2, F, F_c(0.99), F_c(0.999)$	χ^2-test $\chi_1^2, \chi_2^2, \chi_{av}^2, \chi_{0.99}^2, \chi_{0.999}^2$	Variable	A(per cent)
2018.02.17	*R*	45	5.95, 6.20, 6.08	35.41, 38.47, 36.94, 2.04, 2.60	1541.5, 1268.2, 1404.8, 21.7, 27.9	Var	6.10
2018.02.21	*R*	57	6.17, 5.83, 6.00	38.11, 34.02, 36.07, 1.88, 2.32	1496.0, 3079.2, 2287.6, 83.5, 94.5	Var	5.20
2018.04.16	*R*	47	1.60, 1.11, 1.36	2.56, 1.24, 1.90, 2.01, 2.54	90.2, 176.9, 133.5, 71.2, 81.4	NV	–
2018.04.17	*R*	52	2.54, 2.60, 2.57	6.46, 6.70, 6.58, 1.94, 2.42	267.0, 1091.8, 679.4, 77.39, 87.97	Var	9.10
2018.05.05	*R*	84	1.80, 2.27, 2.03	3.25, 5.14, 4.20, 1.67, 1.99	215.5, 1088.8, 652.1, 115.9, 128.6	Var	9.10
2018.05.06	*R*	78	3.92, 3.17, 3.55	15.43, 10.05, 12.74, 1.71, 2.04	865.2, 1816.7, 1340.9, 108.8, 121.1	Var	13.90
2018.05.13	*R*	23	1.88, 2.04, 1.96	3.53, 4.17, 3.85, 2.78, 3.98	1.8, 2.2, 2.0, 40.29, 48.27	NV	–
	I	17	2.43, 2.16, 2.30	5.90, 4.68, 5.29, 3.37, 5.20	2.8, 2.3, 2.5, 32.0, 39.2	NV	–

Notes. Var: variable, NV: non-variable.
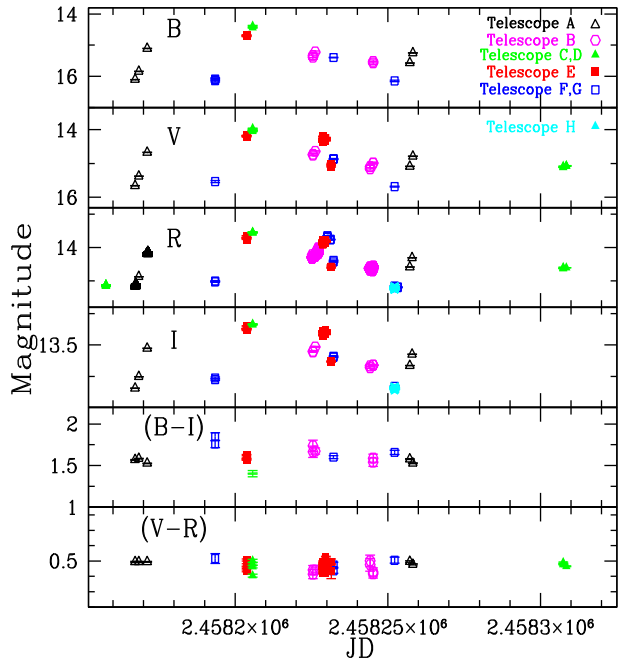
Figure 2. Short-/long-term variability LCs and colour indices of 3C 279 in the *B*, *V*, *R*, and *I* bands and (*B* − *I*) and (*V* − *R*) colours. Different colours denote data from different observatories: black, HCT (Telescope A); magenta, ARIES (Telescopes B); green, JS (Telescopes C and D); red, HSH (Telescope E); blue, Bulgaria (Telescopes F and G); Cyan, Turkey (Telescope H).

Table 4. Results for STV studies displaying magnitude changes in each band.

Band	Faintest Mag	Date (Max)	Brightest Mag	Date (Min)
B	16.15	2018.05.13	14.38	2018.03.28
V	15.68	2018.05.13	13.96	2018.03.28
R	15.25	2018.05.13	13.54	2018.03.28
I	14.58	2018.05.13	12.99	2018.03.28

Notes. Column 1 indicates the band in which observations were taken, column 2 represents the maximum magnitude attained by the source in the filter given in column 1 on a particular date, which is mentioned in column 3, followed by the minimum magnitude value and respective date in columns 4 and 5.

date, column 2 gives the filter in which observations were carried out, number of data points in a particular filter are given in column 3, results of *C*-, *F*-, and χ^2-tests are given in columns 4, 5, and 6, respectively, column 7 tells if the source is variable or not, and column 8 gives variability amplitude.

We found noticeable STV in case of *B*, *V*, *R*, and *I* passbands. Our source seems to have reached the faintest state in *B*, *V*, *R*, and *I* filters on 2018 May 13 as clearly evident from the LC in Fig. 2. The flux from the blazar was found to increase after 2018 May 13 for the next few days. During our observation run, 3C 279 reached the brightest *R*-band magnitude of 13.54 that is just ∼0.94 mag fainter than its flux level of *R* ∼ 12.6 reported by Gupta et al. (2008) when the source was in an outburst state. The source decayed significantly reaching *R* ∼ 15.25, which is still brighter than its faint state of *R* ∼ 17.1 reported by Rani et al. (2010). Above results are summarized in Table 4.

To calculate the variability amplitude in each filter during the entire monitoring period, we used equation (4). The STV amplitude was found to increase with frequency, with the following values: ∼177 per cent, ∼172 per cent, ∼171 per cent, and ∼158 per cent in *B*, *V*, *R*, and *I* bands, respectively, which is in accordance with other investigators (Ghiselini et al. 1997; Papadakis et al. 2003; Bonning et al. 2012). Such a trend is dominant when substantial variability is present over the observation duration. A few possible scenarios of optical emission include the standard shock-in-jet model (e.g. Marscher & Gear 1985; Spada et al. 2001; Joshi & Böttcher 2011), colliding plasma shells (e.g. Guetta et al. 2004), variations in the direction of forward beaming (e.g. Villata & Raiteri 1999), and many more. The most promising scenarios for flux variations in blazars from intraday to long time-scales is the shock-in-jet model, where shocks from the base of jet travelling down the Doppler-boosted relativistic jet induce significant flux fluctuations, accelerating particles and/or compressing magnetic field (Marscher 2014). Thermal emissions in the optical scenario could be associated with the AD instabilities such as hotspots when the source is in the low brightness state (Chakrabarti & Wiita 1993; Mangalam & Wiita 1993). STV of blazars is also well modelled in terms of the helical jet model (Marscher & Travis 1996). Variations in viewing angle might also account for changes in the source brightness. At larger viewing angles, the source is fainter while at a smaller angle it is brighter (Lainela et al. 1999). We also investigated corresponding (*B* − *I*) and (*V* − *R*) variations on short-term basis. Colour variations with time are displayed in the lower two panels of Fig. 2. The variability amplitude for (*B* − *I*) was calculated to be 0.47 per cent with a maximum value of 1.84 and a minimum of 1.38 mag, while the amplitude of variability for (*V* − *R*) was estimated to be 0.12 per cent for a maximum of 0.52 and a minimum of 0.40 mag. Larger (*B* − *I*) values are expected owing to increase in standard deviation with frequency separation between two bands.
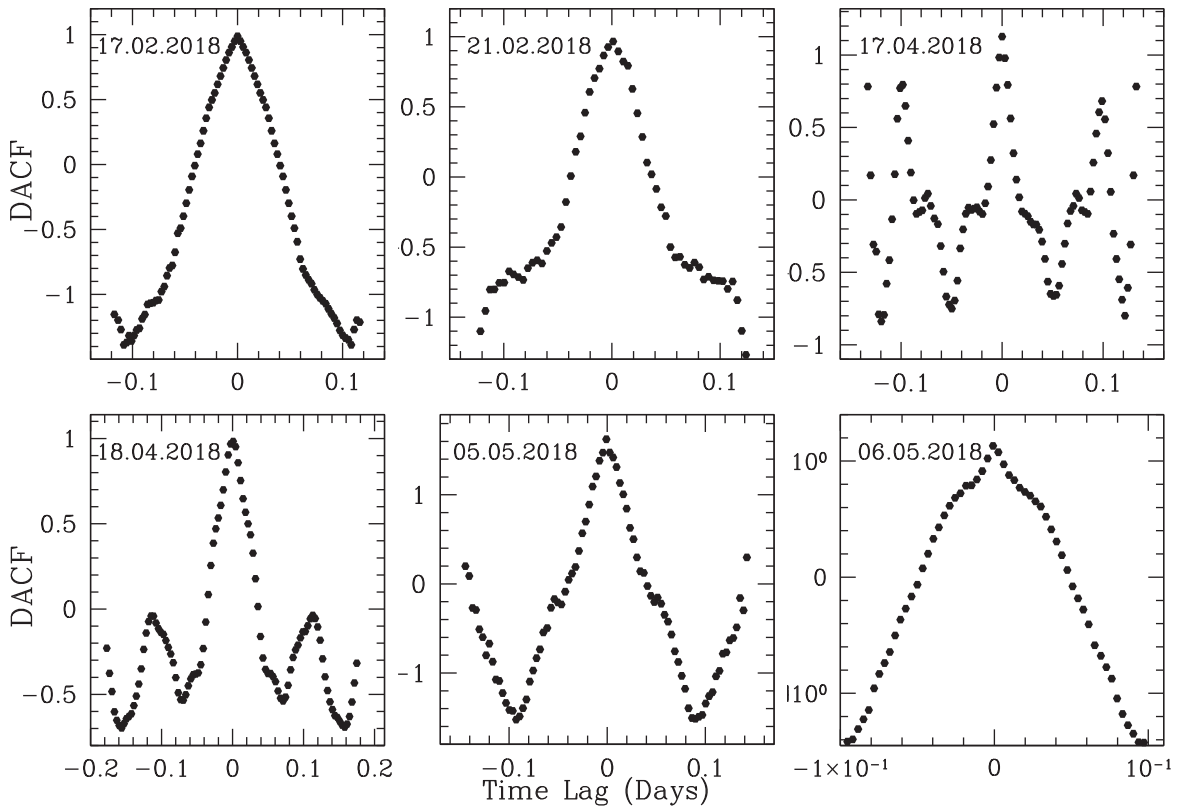
4.1 Variability time-scales

To quantitatively calculate time-scale of variations in the optical fluxes, we used SF and DACF techniques as explained in Sections 3.5 and 3.6. We have constructed DACFs and SFs for all those observation dates when the source was found to be variable. SFs are displayed in Fig. 3, while DACFs are shown in Fig. 4.

The SF for 2018 February 17 displays a monotonic increase with no detectable plateau that implies that variability time-scales are longer than the observation span. Similarly, the DACF also did not display any significant trend. For February 21, we have a double hump appearance in the SF plot at ∼87 and ∼202 min. As evident from the plot, plateau was not followed by any dips, thus these time-scales cannot be considered significant and could be due to photometric and systematic errors on the data points. Similar trend with same time-scale values was found by DACF analysis also. The LC for the night of April 17 shows indications of three humps and two dips with characteristic variability time-scales of 72, 108, and 173 min. Dips provide evidence of quasi-periodicity in the LC. To cross-check for the presence of these detected time-scales of variability, we performed DACF analysis. As evident from the Fig. 4, similar variability time-scales were detected from DACF analysis along with hints of quasi-periodicity. The nominal time-scales of variability for April 18 were found to be about 23, 100, and 200 min. Similar trends were suggested by SF plot of May 05 displaying two plateaus and dips. For May 05, we detected possible variability time-scales of ∼60 and 120 min. The first dip of the SF might hint towards periodicity in the LC, but as the
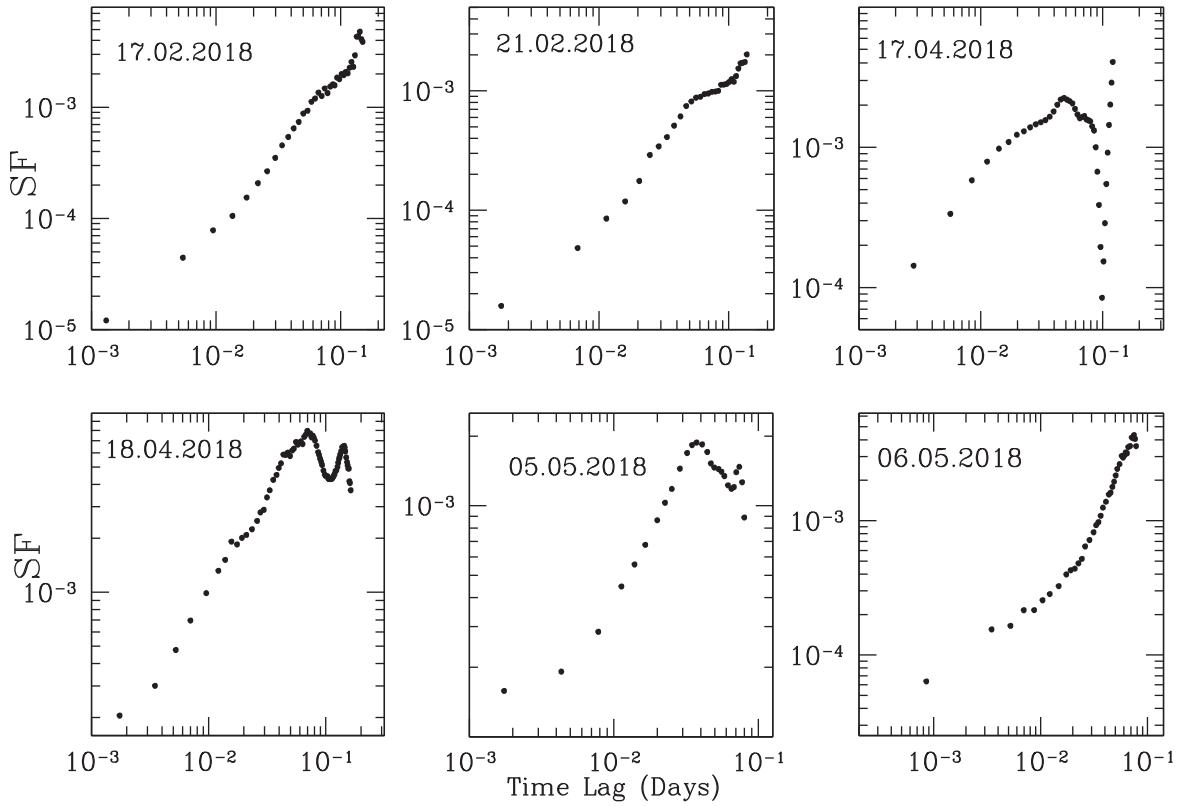
Figure 3. SF plots for the blazar 3C 279 in the *R* passband. Observation date is indicated in each plot. In each plot, *x*- and *y*-axis are the time lag (days) and SF values, respectively.

Figure 4. DACF plots for the blazar 3C 279 in *R* passband. Observation date is indicated in each plot. In each plot, *x*- and *y*-axes are the time lag (days) and DACF values, respectively.

Table 5. Time-scales of the intranight variability and the corresponding upper limits of the emission region sizes (au = astronomical units).

Date of observations (yyyy mm dd)	Time-scale (min)	Size ($\times 10^{15}$ cm)	(au)
2018 02 21	87	1.19 ± 0.18	79 ± 12
2018 04 17	72	0.98 ± 0.15	66 ± 10
2018 04 18	23	0.31 ± 0.05	21 ± 3
2018 05 05	60	0.82 ± 0.12	55 ± 8
2018 05 06	115	1.57 ± 0.24	105 ± 16

subsequent dips are absent, the detected periodicities cannot be considered significant. The nominal variability time-scales for April 18 and May 05 were supported by DACF technique also. SF plot for May 06 displays a continuously rising trend giving a possible variability time-scale of 115 min. Since the plateau was not followed by any dips, any variability time-scale is greater than or equal to the observation duration. Also, SF results were not supported by DACF analysis and hence are not reliable.

Variability time-scales can be used to find the size of the emitting region or the Eddington luminosity. To relate observed quantities with the rest-frame quantity, we make use of Doppler boosting factor

$$\delta = \frac{1}{\Gamma(1 - \beta \cos\theta)}, \tag{9}$$

where θ is the angle which the LOS makes with the jet axis, $\beta = v/c$, with v being the velocity of the plasma in the jet and c is the velocity of light in vacuum, while Γ is the bulk Lorentz factor of flow which is given as $\Gamma = [1 - \beta^2]^{-1/2}$. Shortest time-scale of variability is proposed to be associated with the light crossing time. The size of the emitting region is given as $R \leq c\,\delta\Delta t/(1 + z)$. Chen ([2018](#)) obtained Doppler factor of 27.7 by fitting the NASA/IPAC Extragalactic Database (NED)[3] generated SED with a one – zone synchrotron+IC model. However, given the non-simultaneity of the SEDs fitted, the estimated parameters of a single object have to be considered with some caution. Jorstad et al. ([2017](#)) calculated individual Doppler factors for a set of knots using their kinematic data related to the knots ejected before 2013. The weight-averaging of the individual measurements results in a Doppler factor of 15.3 ± 3.9 (weighted standard deviation of 7.5). Liodakis et al. ([2018](#)) calculated Doppler factor of $11.64^{+1.11}_{-1.77}$ using a Bayesian approach to model the 2008–2017 radio curve of 3C 279. This result could be considered as an average Doppler factor for that period and it is in good agreement with the mean Doppler factor estimated from the kinematic data. Moreover, the modelled curves are very close in time to our monitoring campaign. So, we shall use the so obtained Doppler factor in our further consideration.

For each night, we derived the minimal time-scale as the first plateau/maximum of SF. Using the estimated time-scales and the Doppler factor of 11.64, we calculated the upper limits of the size of the regions responsible for the intranight variability (Table [5](#)). Time-scales of variability detected during our observation run ranged from 23 to 115 min. Ackermann et al. ([2016](#)) detected a significant flux variability at suborbital time-scales of ~ 5 min using the Fermi–LAT observations. Variability time-scales as short as ~ 5 min in gamma-rays can be explained by mirror-driven clumpy jet model or/and model based on synchrotron origin from a magnetically dominated

jet. More detections of minute scale variability time-scales will help to disentangle the theory behind various blazar emission models.

The estimated sizes of the emitting regions for 3C 279 are consistent with those found for other blazars. For example, Kaur et al. ([2017](#)) found sizes in the range of 7.0×10^{14}–3.5×10^{15} cm over a period of 10 yr for 3C 66A. The continuous, 72 h long LC of S5 0716+714 (Bhatta et al. [2013](#)), provided an unique opportunity to model flares with synchrotron pulses and to estimate sizes of the turbulent cells in a consistent way – the sizes reported cover a range from 9.0×10^{13} to 2.5×10^{15} cm. Rafle, Webb & Bhatta ([2012](#)) applied the above model to $\sim$6-yr long campaign on S5 0716+714 (Montagni et al. [2006](#)) and obtained the cell sizes in the range of 6.0×10^{13}–1.0×10^{15} cm. Based on these literature estimates (in addition to ours), we could claim that the typical size of the regions responsible for the intranight variability lies in the range of 6.0×10^{13}–3.5×10^{15} cm. The precision of the these limits could be further increased if we enlarge the number of the independent size estimates. This, however, is beyond the scope of this paper. In addition, the modelling of Rafle et al. ([2012](#)) and Bhatta et al. ([2013](#)) revealed that almost all of the turbulent cells are with sizes less than $\sim 7.5 \times 10^{14}$ cm.

The turbulence is a stochastic process and each intranight LC is a particular realization of this process. Therefore, increasing of the number and quality of intranight LCs we could gain a knowledge about the turbulence in the relativistic plasma. In the framework of Kolmogorov theory, the smallest scales probe the regions where the viscous dissipation of turbulence kinetic energy takes place (the so-called Kolmogorov scale, a smallest scale in a turbulent flow); the largest scales mark the regions of the energy injection in the turbulent region. Based on the above considerations, we could state that the upper limit for the Kolmogorov scale in blazar jets is 6.0×10^{13} cm. This is a rough estimate and it should be made more precise increasing the number independent size estimates.

The sizes of the regions responsible for intranight variability are much smaller than those used in the SED modelling, which are typically of about 10^{17} cm (e.g. Banerjee et al. [2019](#)). In any case, the maximal intranight time-scales set an lower limit on the jet size.

4.1.1 The composite April 18 flare

Among the intranight LCs shown in Fig. [1](#), the most complicated is that one on April 18. The other multipeaked LCs were observed on April 17 and May 05. The April 17 LC shows somewhat flat-topped flares, which can be a result of the single flares overlapping, whereas the May 05 LC is too noisy. So, we shall consider in details only the April 18 LC.

At the beginning of the monitoring on April 18, the source fades by $\sim$0.7 mag within $\sim$30 min. This fading is followed by four overlapping flares. After the last flare – near the end of the monitoring – the flux slightly increases and shows some fluctuations. We, however, cannot make a firm conclusion what this feature is because of the end of the observing set. The first flare peaks at $\sim$17.4 h UT, and the effect of the flare on to the SF could be seen as a local maximum at $\sim$0.015 d or $\sim$23 min. To get information about the characteristics of the flares we decomposed the intranight LC using a sum of four double exponential functions (see Abdo et al. [2010](#)). We excluded from the fit the initial fading and the final brightening of the source and assumed the flux level underlying the flares to be constant. The flares were fitted simultaneously using the weighted least-squares fitter MPFIT (Markwardt [2009](#)). The decomposition is shown in Fig. [5](#). In the further discussion, we
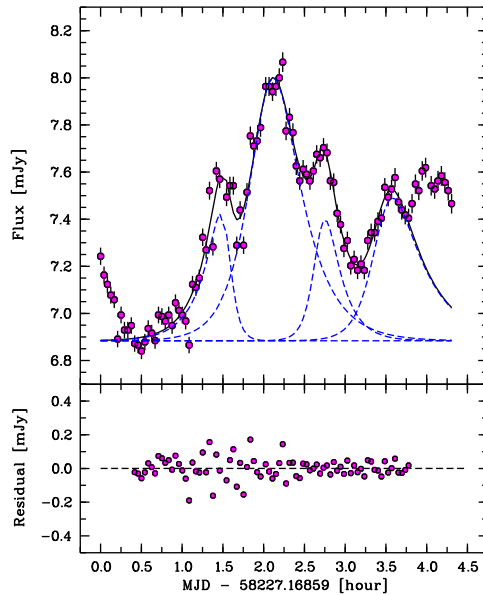
Figure 5. Decomposition of the April 18 flare. The fitting residuals have a standard deviation of 0.06 mJy.

Table 6. CM dependences and CM correlation coefficients on short time-scales.

Colour indices	m	c	r	p
$(B - I)$	0.092	1.228	0.301	0.210
$(B - V)$	0.027	1.409	0.139	0.571
$(R - I)$	0.036	0.600	0.362	0.024
$(V - R)$	0.015	0.248	0.301	0.042

Notes. m = slope and c = intercept of CI against V; r = Spearman coefficient; p = null hypothesis probability.

Figure 6. CM plots on short time-scales for 3C 279. The V magnitudes are given on the x-axis and various colour indices are plotted against them.

shall exclude the decay time-scale of the first flare and the rise time-scale of the third flare owing to the small number of data points covering the corresponding phases of the flares.

The fitted rise (*e*-folding) time-scales of the individual flares were found to be consistent to each other to within the formal uncertainties. The same applies for the decay time-scales as well. In addition, the decay time-scales were found to be systematically larger than the rise ones yet consistent with them to within the uncertainties. We derived the weighted mean (over the individual flares) rise and decay time-scales in the observer's frame to be (13.5 ± 2.5) min, $\chi^2_{\rm df} = 0.7$, and (14.6 ± 6.0) min, $\chi^2_{\rm df} = 0.9$, respectively, where the uncertainties quoted are the weighted standard deviation about the weighted mean. We shall assume that the flares are symmetric based on these weighted mean results. The obtained mean rise time-scale is consistent with that one obtained if we consider the local maximum on the corresponding SF, the latter being, however, more conservative estimate. The flares symmetry could mean either the injection time is comparable while the cooling time is shorter than the light crossing time (Chiaberge & Ghisellini 1999), or geometric effects are in play. Unfortunately, this issue cannot be resolved owing the lack of multiband LCs for April 18.
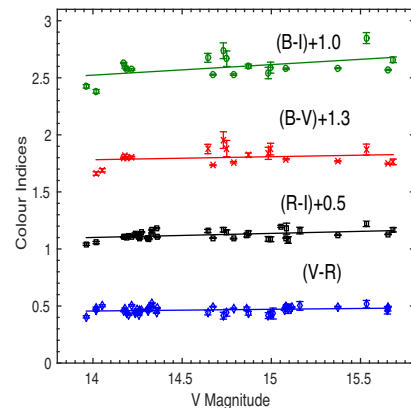
Let us assume that the individual flares are produced by turbulent cells which cool by synchrotron emission after being hit by a strong shock (see below). Then the multiple overlapping flares observed on April 18 could mean that the shock hits a fragmented region within the jet, consisting of at least four distinct cells; it is worth mentioning in this context. Rafle et al. (2012) who assumed the outliers in their cell sizes distribution could be an unresolved group of cells rather than a single one. We obtained an upper limit of the size of this region as $(1.24 \pm 0.10) \times 10^{15}$ cm $= (84 \pm 6)$ au, given the estimated size of a single emitting cell (cf. Table 5). The region size is consistent with the upper limit derived in the previous section.

This kind of multiple fast flares that overlap is not commonly observed during the intranight monitoring campaigns. One of the most spectacular case was captured by Man et al. (2016): they detected five flares within $\sim$70 min. The colour-magnitude diagram

for the composite flare showed strong BWB trend with a hysteresis (Zhang, Wu & Man 2016): a typical feature predicted within the shock-in-jet scenario for blazar's intranight variability (e.g. Kirk, Rieger & Mastichiadis 1998). The BWB trend observed for these flares makes our assumption about the non-geometrical origin of the composite April 18 flare reasonable. The study of such multiple fast flares is of great importance, as they probe the smallest jet scales where the energy dissipates.

4.2 Colour–magnitude relationship

Optical flux variations are accompanied by spectral changes, thus resolving colour–magnitude (CM) relationship can be useful in understanding the origin of blazar emission and also explore various variability scenarios. We now look for any relationship between the colour indices of the source and the brightness in the V band. We fitted the plots of colour indices (CIs) versus V magnitude with straight lines i.e (CI $= m\,V + c$) and calculated the fit values of the slope, m, the constant, c, the Spearman correlation coefficient r along with the corresponding null hypothesis probability, p which are listed in Table 6. A positive slope implies significant positive correlation (when the null hypothesis probability is $p \leq 0.05$) between CI and blazar V magnitude, which in turn implies that the source exhibits a bluer when brighter (BWB) or redder-when-fainter trend (H.E.S.S. Collaboration et al. 2014), while a negative slope implies redder-when-brighter (RWB) trend. A significant positive correlation between V-band magnitude and colour indices on few months time-scales was detected for $(R - I)$ and $(V - R)$, while no clear trend was observed for $(B - I)$ and $(B - V)$, as evident from Table 6. A CM plot for short time-scales is shown in Fig. 6. In Fig. 6, offset values of 1.0, 1.3, and 0.5 are used with $(B - I)$, $(B - V)$ and $(R - I)$, respectively, for clarity.

Colour behaviour obtained by us is similar to Raiteri et al. (2003). They also found weak BWB trends on few instances only. BWB trend has been predominantly observed in blazars by most of the optical observations (Ghosh et al. 2000; Clements & Carini 2001; Gu et al. 2006; Rani et al. 2010; Agarwal & Gupta 2015; Gupta et al. 2016) that was also exhibited by our quasi-simultaneous observations. As given by Sasada et al. (2010), CM relationship in blazars varies among different states of the source, i.e. outburst state, active state, and faint state. During our observation run, we found that the source attained the maximum flux level of 13.537 mag in *R* passband, which is just ∼0.94 mag fainter than its brightest known magnitude of $R \sim 12.6$ (Gupta et al. 2008). Therefore, most likely we observed the source in a post-outburst state. Among the above-mentioned three states, we can best describe the source as being in active state and thus the colour trend obtained by us is in agreement with those reported by Sasada et al. (2010). No clear trends have been detected by several authors (Stalin et al. 2006; Böttcher et al. 2007; Agarwal et al. 2016).

The average spectral indices are calculated using the following relation (e.g. Wierzcholska et al. 2015),

$$\langle \alpha_{BR} \rangle = \frac{0.4 \langle B - R \rangle}{\log(\nu_B / \nu_R)}, \tag{10}$$

where ν_B and ν_R are effective frequencies of the respective bands (Bessell, Castelli & Plez 1998).

The optical slope for all nights, when quasi-simultaneous observations in *B*, *V*, *R*, and *I* filters were taken, were calculated using equation (10) and were found to range between 2.3 ± 0.05 and 3.0 ± 0.03. These steep spectral index values imply strong synchrotron emission from the Doppler boosted blazar jet. Optical emission from blazars can be explained by different theoretical models, namely AD based model and the shock-in-jet model. According to the Blandford & Rees (1978) model, non-thermal emission in case of blazars is associated with the relativistic Doppler boosted jet pointed towards the observer's direction. Therefore, optical emission from blazars can be attributed to the shock-in-jet models. It is expected that the charged particles in the active regions propagating along the jet are accelerated to very high energies.

Optical flux variations in blazars are often accompanied by colour variations. Colour variability trends in blazars is still a matter of debate. Some authors have detected a bluer-when-brighter trend (e.g. Ghosh et al. 2000; Raiteri et al. 2001; Villata et al. 2002; Gu et al. 2006; Agarwal & Gupta 2015; and references therein), while some others have claimed the opposite, i.e. RWB trend (e.g. Raiteri et al. 2007; Gaur, Gupta & Wiita 2012). Densely sampled, high-precision, and simultaneous multifrequency data will be helpful to clearly know the CM relationship in blazars on short-term basis and will also help in constraining blazar variability models.

We also studied SED changes associated with our source, corresponding to the observed flux variations along four optical bands. Based on the location of low-energy peak in blazar SED, we have low-energy peaked blazars (LBLs), intermediate-energy peaked blazars (IBLs), and high-energy peaked blazars (HBLs). For HBLs, the synchrotron component peaks in the X-ray range, for IBLs it lies in the optical-UV range, and for LBLs in the infrared region. FSRQs are found to be exclusively low-energy peaked with synchrotron peak located close to optical wavelengths, thus optical variability studies assist in constraining various theoretical models. They also provide information on the emitting region of relativistic electrons, as SED changes are most likely caused by variations in the spectra of emitting electrons, which are further caused from differences in the physical parameters of relativistic jets. The optical
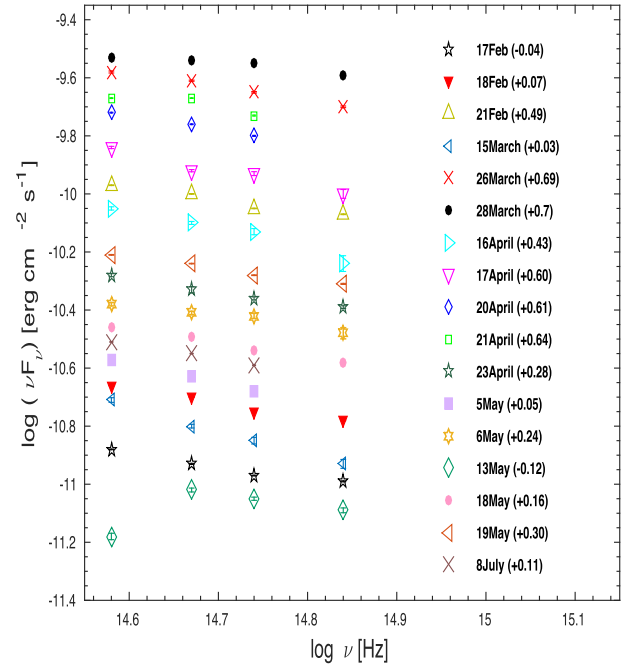
Figure 7. SED results for 3C 279 in optical frequency range. Different symbols are used for each epoch. The offset used to clearly display SED plot for each date is also mentioned along the date as shown in the figure.

synchrotron spectra of blazars follow single power law: $F_\nu \propto \nu^{-\alpha}$, with α being the optical spectral index.

We used our quasi-simultaneous *B*, *V*, *R*, and *I* data sets and generated 17 optical SEDs for the source spanning 2018 February to 2018 July. We de-reddened the calibrated magnitudes of 3C 279 by subtracting Galactic absorption $A_B = 0.104$ mag, $A_V = 0.078$ mag, $A_R = 0.062$ mag, and $A_I = 0.043$ mag (Cardelli, Clayton & Mathis 1989). Fig. 7 displays quasi-simultaneous narrow-band optical SEDs of 3C 279, corresponding to 17 different epochs during the observation span. The faintest fluxes for our target were measured on 2018 May 13 and the maxima was observed on 2018 March 28, while significant variations were detected on other days as evident from the figure. Due to lack of multiwavelength observations, we were not able to explore SED changes further. Multiwavelength SEDs can also provide vast amount of information about physical parameters of the emitting region.

5 DISCUSSION

Blazars, being at cosmological distances, cannot be completely resolved using present observational techniques. Even the high-resolution radio telescopes are still not capable of resolving the jet formation region close to the central engine. Thus, investigating variability on diverse time-scales will help us to better understand these objects. Various intrinsic and extrinsic models have been reported to account for temporal variability in blazars. The intrinsic origin of variability could be either due to relativistic jet or AD instabilities. While the extrinsic ones involve interstellar scintillation (ISS; dominant at low-frequencies), geometrical effects (Gopal-Krishna & Wiita 1992) occurring within the jet and gravitational microlensing (Chang & Refsdal 1979; Bignall et al. 2003). Since blazar emission is generally dominated by Doppler boosted non-thermal radiation from the relativistic jet, variability on wide range of time-scales can be explained by the jet based models. Flaring

activities in blazars on intraday and short time-scales could arise due to the emergence and propagation of a new shock that could be due to variations in the velocity, electron density, or magnetic field of the Doppler boosted relativistic jet. Moreover, optical IDV/STV of blazars can be explained by various models involving irregularities in the jet flow due to ongoing shock; turbulence behind the shock; variations in the outflow parameters due to magnetic reconnection and turbulence (e.g. Marscher 2014; Calafut & Wiita 2015; Sironi, Petropoulou & Giannios 2015).

We found a mild BWB trend during our observation span. BWB trend in blazars can be explained by the presence of two components, a variable one having a flatter slope (α; $f_\nu \propto \nu^{-\alpha}$) and another stable one with $\alpha_{\mathrm{const}} > \alpha$ contributing to overall emission at optical wavelengths. The variable component contributes to the chromatic behaviour of the source. Alternatively, the observed BWB trend can be explained in terms of one-component synchrotron model (Fiorucci, Ciprini & Tosti 2004) according to which the emission is boosted to higher frequencies, as the energy release is intense. Studying the behaviour in different optical bands can help us estimate the type of origin for the variability. Increasing variability amplitude with frequency can be mostly explained by the accelerated electrons at the shock front which then loose energy while propagating away from the front. Owing to synchrotron cooling, the high-frequency electrons loose energy faster than the low-frequency ones. Due to the closeness of energy bands in the optical regime, a flare should be initiated simultaneously at all optical wavebands; thus, observations on short time-scales could miss the detection of the time lags among various optical bands. The above emission behaviour of the source was found to be consistent in all four passbands, thus suggesting that B, V, R, and I emissions come from the same region and by the same physical process. The present optical data sets for the source can be correlated with the observations at other wavelengths to investigate its behaviour over the entire EM spectrum.

6 CONCLUSIONS

In this paper, we presented our optical monitoring work that targeted the blazar, 3C 279, observed with seven different telescopes between 2018 February and 2018 July. This helped in studying the intraday to long-term flux and colour variability of this source to understand its nature in the optical regime. We gathered about 716 optical B, V, R, and I frames for 3C 279. The analysis of the data revealed that the source was active during the entire monitoring period.

(i) 3C 279 was found to be variable on five out of seven nights on intraday time-scales. The source displayed IDV amplitudes ranging from 5.20 per cent to 17.90 per cent between 2018 February to July.

(ii) All optical passbands (B, V, R, and I) clearly displayed flux variability on short time-scales, while colour variability was found to be very weak.

(iii) The STV amplitude was found to increase with frequency, similar to the results of Papadakis et al. (2003). The maximum variability amplitude was found in the B passband of around 177 per cent.

(iv) The source depicted a small flare peaking around 2018 March 28 and later attained the faintest state around 2018 May 13, while was found to again brighten afterwards. Unfortunately, due to several observational constraints we could not obtain data samples to cover this brightening phase of 3C 279.

(v) The above emission behaviours of the source were found to be consistent in all four passbands, thus suggesting that B, V, R, and

I emissions come from the same region and by the same physical process that is expected due to the closeness of the bands.

(vi) Using SF analysis, we found shortest variability time-scale of 23 min while the highest reaching upto 115 min. Our claim of the variability event on 2019 April 18, over a time-scale of ∼23 min has a low amplitude of ∼17.90 per cent (Cellone, Romero & Araudo 2007). Also, we have accounted for error sources involved in aperture photometry followed by quantitative analysis of any detected variations; thus, we can firmly establish that we have detected a real variability time-scale.

(vii) The shortest variability time-scale of 23 min gives a lower limit on the size of emission region of about 0.31×10^{15} cm.

(viii) We also studied correlation between the colour indices of the target and its V band magnitude and found that BWB trend was dominant on short time-scales.

(ix) Optical spectral indices ranged from 2.3 to 3.0 but displayed no clear trend with time during our observation span. We generated 17 optical SEDs using quasi-simultaneous B, V, R, and I observation points and found the faintest SED on 2018 May 13, while the brightest was observed on 2018 March 28. Significant variations were observed between the brightest and the faintest SED.

To further understand, the variability on diverse time-scales for our target 3C 279 in the optical window, densely sampled observations are encouraged. Above optical data sets for the source can be correlated with the observations at other wavelengths to investigate its behaviour over the entire EM spectrum. In addition to that, simultaneous multifrequency data will help us model various emission mechanisms and constrain the theoretical models.

REFERENCES

Abdo A. A. et al., 2010, ApJ, 722, 520
Acero F. et al., 2015, ApJS, 218, 23
Ackermann M. et al., 2016, ApJ, 824, L20
Agarwal A., Gupta A. C., 2015, MNRAS, 450, 541
Agarwal A. et al., 2015, MNRAS, 451, 3882
Agarwal A. et al., 2016, MNRAS, 455, 680
Andruchow I., Cellone S. A., Romero G. E., Dominici T. P., Abraham Z., 2003, A&A, 409, 857
Banerjee B., Joshi M., Majumdar P., Williamson K. E., Jorstad S. G., Marscher A. P., 2019, MNRAS, 487, 845

Begelman M. C., Blandford R. D., Rees M. J., 1984, Rev. Mod. Phys., 56, 255

Bessell M. S., Castelli F., Plez B., 1998, A&A, 333, 231

Bhatta G. et al., 2013, A&A, 558, A92

Bignall H. E. et al., 2003, ApJ, 585, 653

Blandford R. D., Königl A., 1979, ApJ, 232, 34

Blandford R. D., Rees M. J., 1978, Phys. Scr., 17, 265

Blinov D. et al., 2015, MNRAS, 453, 1669

Bonning E. et al., 2012, ApJ, 756, 13

Böttcher M. et al., 2007, ApJ, 670, 968

Böttcher M., Reimer A., Sweeney K., Prakash A., 2013, ApJ, 768, 54

Calafut V., Wiita P. J., 2015, JA&A, 36, 255

Cardelli J. A., Clayton G. C., Mathis J. S., 1989, ApJ, 345, 245

Cellone S. A., Romero G. E., Araudo A. T., 2007, MNRAS, 374, 357

Chakrabarti S. K., Wiita P. J., 1993, ApJ, 411, 602

Chang K., Refsdal S., 1979, Nature, 282, 561

Chatterjee R. et al., 2008, ApJ, 689, 79

Chen L., 2018, ApJS, 235, 39

Chiaberge M., Ghisellini G., 1999, MNRAS, 306, 551

Clements S. D., Carini M. T., 2001, AJ, 121, 90

Cohen M. H., Cannon W., Purcell G. H., Shaffer D. B., Broderick J. J., Kellermann K. I., Jauncey D. L., 1971, ApJ, 170, 207

Collmar W. et al., 2007, ESASP, 622, 207

de Diego J. A., 2010, AJ, 139, 1269

Edelson R. A., Krolik J. H., 1988, ApJ, 333, 646

Fan J. H., Lin R. G., 2000, ApJ, 537, 101

Fan J.-H., Romero G. E., Wang Y.-X., Zhang J.-S., 2005, ChJAA, 5, 457

Fiorucci M., Ciprini S., Tosti G., 2004, A&A, 419, 25

Gaur H., Gupta A. C., Wiita P. J., 2012, AJ, 143, 23

Gaur H., Gupta A. C., Lachowicz P., Wiita P. J., 2010, ApJ, 718, 279

Ghisellini G. et al., 1997, A&A, 327, 61

Ghosh K. K., Ramsey B. D., Sadun A. C., Soundararajaperumal S., Wang J., 2000, ApJ, 537, 638

Giommi P., Padovani P., Polenta G., Turriziani S., D'Elia V., Piranomonte S., 2012, MNRAS, 420, 2899

Gopal-Krishna, Wiita P. J., 1992, A&A, 259, 109

Gopal-Krishna, Stalin C. S., Sagar R., Wiita P. J., 2003, ApJ, 586, L25

Gu M., Cao X., Jiang D. R., 2001, MNRAS, 327, 1111

Gu M. F., Lee C.-U., Pak S., Yim H. S., Fletcher A. B., 2006, A&A, 450, 39

Guetta D., Ghisellini G., Lazzati D., Celotti A., 2004, A&A, 421, 877

Gupta A. C., Banerjee D. P. K., Ashok N. M., Joshi U. C., 2004, A&A, 422, 505

Gupta A. C. et al., 2008, AJ, 136, 2359

Gupta A. C. et al., 2016, MNRAS, 458, 1127

H.E.S.S. Collaboration et al., 2014, A&A, 571, AA39

Heidt J., Wagner S. J., 1996, A&A, 305, 42

Hunger L., Reimer A., 2016, A&A, 589, A96

Jockers K. et al., 2000, KFNTS, 3, 13

Jorstad S. G. et al., 2005, AJ, 130, 1418

Jorstad S. G. et al., 2017, ApJ, 846, 98

Joshi M., Böttcher M., 2011, ApJ, 727, 21

Kaur N., Sameer, Baliyan K. S., Ganesh S., 2017, MNRAS, 469, 2305

Kirk J. G., Rieger F. M., Mastichiadis A., 1998, A&A, 333, 452

Königl A., 1981, ApJ, 243, 700

Lachowicz P., Czerny B., Abramowicz M. A., 2006, preprint (arXiv:astro-ph/0607594)

Lainela M. et al., 1999, ApJ, 521, 561

Lindfors E. J. et al., 2006, A&A, 456, 895

Liodakis I., Hovatta T., Huppenkothen D., Kiehlmann S., Max-Moerbeck W., Readhead A. C. S., 2018, ApJ, 866, 137

Lynds C. R., Stockton A. N., Livingston W. C., 1965, ApJ, 142, 1667

MAGIC Collaboration et al., 2008, Science, 320, 1752

Man Z., Zhang X., Wu J., Yuan Q., 2016, MNRAS, 456, 3168

Mangalam A. V., Wiita P. J., 1993, ApJ, 406, 420

Maraschi L. et al., 1994, ApJ, 435, L91

Markwardt C. B., 2009, ASPC, 411, 251

Marscher A. P., 2014, ApJ, 780, 87

Marscher A. P., Gear W. K., 1985, ApJ, 298, 114

Marscher A. P., Travis J. P., 1996, A&AS, 120, 537

Montagni F., Maselli A., Massaro E., Nesci R., Sclavi S., Maesano M., 2006, A&A, 451, 435

Mücke A., Protheroe R. J., Engel R., Rachen J. P., Stanev T., 2003, Astropart. Phys., 18, 593

Nilsson K., Pursimo T., Villforth C., Lindfors E., Takalo L. O., 2009, A&A, 505, 601

Papadakis I. E., Boumis P., Samaritakis V., Papamastorakis J., 2003, A&A, 397, 565

Rafle H., Webb J. R., Bhatta G., 2012, J. Southeastern Assoc. Res. Astron., 7, 33

Raiteri C. M. et al., 2001, A&A, 377, 396

Raiteri C. M. et al., 2003, A&A, 402, 151

Raiteri C. M. et al., 2007, A&A, 473, 819

Rani B. et al., 2010, MNRAS, 404, 1992

Romero G. E., Cellone S. A., Combi J. A., 1999, A&AS, 135, 477

Sasada M. et al., 2010, PASJ, 62, 645

Shakura N. I., Sunyaev R. A., 1973, A&A, 24, 337

Simonetti J. H., Cordes J. M., Heeschen D. S., 1985, ApJ, 296, 46

Sironi L., Petropoulou M., Giannios D., 2015, MNRAS, 450, 183

Spada M., Ghisellini G., Lazzati D., Celotti A., 2001, MNRAS, 325, 1559

Stalin C. S., Gopal-Krishna, Sagar R., Wiita P. J., Mohan V., Pandey A. K., 2006, MNRAS, 366, 1337

Stetson P. B., 1987, PASP, 99, 191

Stetson P. B., 1992, ASPC, 25, 297

Unwin S. C., Cohen M. H., Biretta J. A., Hodges M. W., Zensus J. A., 1989, ApJ, 340, 117

Urry C. M., Padovani P., 1995, PASP, 107, 803

Villata M., Raiteri C. M., 1999, A&A, 347, 30

Villata M. et al., 2002, A&A, 390, 407

Wagner S. J., Witzel A., 1995, ARA&A, 33, 163

Wehrle A. E. et al., 1998, ApJ, 497, 178

Wehrle A. E., Piner B. G., Unwin S. C., Zook A. C., Xu W., Marscher A. P., Teräsranta H., Valtaoja E., 2001, ApJS, 133, 297

Wierzcholska A., Ostrowski M., Stawarz Ł., Wagner S., Hauser M., 2015, A&A, 573, A69

Woo J.-H., Urry C. M., 2002, ApJ, 579, 530

Xie G. Z., Zhou S. B., Liang E. W., 2004, AJ, 127, 53

Zhang X., Wu J., Man Z., 2016, Galax, 4, 25

Zibecchi L., Andruchow I., Cellone S. A., Carpintero D. D., Romero G. E., Combi J. A., 2017, MNRAS, 467, 340

This paper has been typeset from a TEX/LATEX file prepared by the author.